Title
Lithospheric instability in obliquely convergent margins: San Gabriel Mountains, southern California

Journal
Journal of Geophysical Research-Solid Earth, 109(B1)

ISSN
0148-0227

Authors
Billen, Magali I
Houseman, G A

Publication Date
2004

Peer reviewed

Lithospheric Instability in Obliquely Convergent Margins: San Gabriel Mountains, S. California

Magali I. Billen* and Gregory A. Houseman

School of Earth Sciences, University of Leeds, Leeds, LS2 9JT, UK.

* Now at University of California, Davis

Short title: LITHOSPHERIC INSTABILITY

Abstract. Oblique convergence across the San Andreas Fault in southern California has lead to rapid uplift of the San Gabriel Mountains since 5 Ma. Tomographic models of this region include a sheet-like, high velocity anomaly, extending to depths greater than 200 km. One proposed mechanism for the formation of this feature is gravitational instability of the lithosphere, resulting in a cold thermal downwelling. We present a systematic study of the sensitivity of lithospheric deformation (lithospheric downwelling, topography, deflection of the Moho, convergent velocity profile) to the viscosity structure in 2-D numerical models of lithospheric instability, including a pre-existing zone of weakness. Strike-parallel strain within a convergent region should create a local zone of weakness due to the non-Newtonian response of the lithosphere. Such a weak zone can focus convergent motion, increasing and localizing the growth-rate of a lithospheric instability. We find that the observed characteristics of deformation depend on the width (x_w) and relative viscous weakening factor (f_w), the ratio of crust to mantle-lithospheric viscosity (η_c/η_m), and the absolute viscosity of the lithosphere (η_m). For the San Gabriel Mountains, we find that a range of models is capable of reproducing the observed Moho deflection and depth extent of the downwelling within the short time since the onset of convergence. However, only a small subset of models, ($x_w = 20$ km, $f_w = 50$–100, $\eta_m = 7.5\times10^{20}$–$1.5\times10^{21}$ Pa s, $\eta_c/\eta_m > 100$) reproduce both the narrow, high topography and horizontal shortening profile.

Introduction

Oblique convergent margins, like that found along the Pacific-North America plate boundary in southern California (Figure 1), comprise a special subset of continental collisions, in that the convergent component of deformation (20 mm/yr) is smaller than the strike-slip component ($>$ 40 mm/yr) [*Crustal Deformation Working Group*, 1998]. In southern California, recent crustal deformation due to convergence along the San Andreas Fault is characterized by a narrow region of deformation with 1) crustal shortening over a 200 km wide region [*Crustal Deformation Working Group*, 1998], 2) rapid uplift of the San Gabriel Mountains (with peaks greater than 3000 m), over a 50 km wide region [*Blythe et al.*, 2000] and 3) crustal thickening by 10–15 km beneath San Gabriel Mountains [*Hafner et al.*, 1996]. This narrow zone of convergent deformation developed since the change in plate motion at about 5 Ma, suggests that the strike-slip strain around the San Andreas Fault system may act to localize the convergent deformation compared to that predicted by models of convergence in laterally homogeneous layers. **Figure 1.**

The recent ($<$ 5 myr) convergent motion across the San Andreas Fault, may have been partially accommodated by removal of some lithospheric-mantle to form a sheet-like, fast seismic velocity anomaly extending to depths of at least 200 km beneath the San Gabriel Mountains of the Transverse Ranges [*Humphreys and Clayton*, 1990; *Hu et al.*, 1994; *Powell and Mitchell*, 1994; *Kohler*, 1999]. Following the initial observations of a fast seismic velocity anomaly beneath the Transverse Ranges [*Hadley and Kanamori*, 1977; *Raikes*, 1980], subsequent studies constrained the lateral and vertical extent of the anomaly to the length of the Transverse Ranges ($>$ 200 km east-west, including the San Bernadino Mountains). The anomaly is centered near the San Gabriel Mountains of the Eastern Transverse Ranges, is approximately 60–120 km wide (north-south), and reaches depths of at least 200 km [*Humphreys and Clayton*, 1990; *Hu et al.*, 1994; *Powell and Mitchell*, 1994; *Kohler*, 1999].

Previous models of regional deformation explained this fast seismic anomaly as either a one-sided slab-like feature caused by subduction of lithosphere from the south [*Bird and Rosenstock*, 1984; *Sheffels and McNutt*, 1986], or as the result of symmetric convective downwelling of lithospheric mantle decoupled from crustal deformation [*Humphreys and Hager*, 1990]. Such models were consistent with the observation at the time, that no crustal thickening existed beneath the Transverse Ranges [*Hadley and Kanamori*, 1977; *Hearn and Clayton*, 1986]. Following recent high-resolution seismic experiments which reveal that the crust is thicker by 10–15 km beneath the San Gabriel Mountains, relative to a regional crustal thickness of 25–35 km [*Hafner et al.*, 1996; *Kohler and Davis*, 1997; *Fuis*, 1998], *Houseman et al.* [2000] developed a quantitative model in which crustal shortening develops with lithospheric downwelling in response to convergence imposed by a surface velocity boundary condition. This type of model is consistent with the observed displacement of the Moho beneath the San Gabriel Mountains and the present-day geodetic strain field. It also depends on the idea that the continental lithospheric mantle may be gravitationally unstable, as has been suggested in different contexts by authors who have proposed mechanisms such as delamination [*Bird*, 1978, 1979], lithospheric-mantle subduction [*Beaumont et al.*, 1994; *Willet and Beaumont*, 1994], and convective thinning [*Houseman et al.*, 1981].

Like previous models of lithospheric instability, the models of *Houseman et al.* [2000]

require a low lithospheric viscosity (less than about 2.0×10^{20} Pa s) in order for the downwelling to develop in less than 5 million years, as constrained by the plate boundary history. Furthermore, while they suggested that the localization of deformation near the plate boundary could be due to the non-Newtonian response of the lithosphere, they did not include lateral variations of lithospheric viscosity in their calculations. Rather they enforced localization of deformation by imposing a surface velocity profile consistent with that observed (Figure 1B). The possible importance of pre-existing weak regions on the deformation in oblique margins has also been considered in the similar geologic setting of the Southern Alps, New Zealand [*Gerbault et al.*, 2003], although the importance of strike-parallel deformation in maintaining the weak zone and affecting the convergent deformation is not considered.

Here we first discuss a simplified analytic model for deformation in a sheared thin viscous sheet. This model provides a rationale for the horizontal variation in lithospheric strength that may cause localization of the convergence. We then investigate how deformation due to imposed convergence depends on the lithospheric-mantle viscosity, its lateral variation as described by the length-scale and degree of weakening near the plate boundary, and the crust to lithospheric-mantle viscosity ratio. In these 2-D convergence experiments, deformation is localized by the lateral variation in viscosity, rather than by a surface velocity boundary condition. Our numerical experiments are constrained by observations of the fast seismic velocity anomaly, variation of crustal thickness, the convergent velocity profile and topographic profile of the San Gabriel Mountains. Our aim is to determine if these observations are consistent with this mechanism in which lithospheric downwelling, crustal thickening and topographic uplift have developed in response to plate boundary convergence acting on a zone of lithospheric weakness; and if so, what is the viscosity structure necessary to match the set of observations?

Thin Sheet Model of Lithospheric Viscosity Variation

The oblique convergent margin of southern California is dominated by motion in the strike-parallel direction, with a relative velocity ($u = 40$ mm/yr) two to three times that in the strike-normal direction ($v = 15 - 20$ mm/yr). Note that relative plate motions based on the NUVEL-1 plate reconstruction model [*de Mets et al.*, 1990] are slightly greater in magnitude than measurements based on GPS data within 150 km of the San Andreas Fault. These two components of motion are orthogonal, and the associated strain-fields may therefore be computed separately if variation in the along-strike direction is slow, and if the flow is Newtonian. The viscosity structure influencing each component of motion will depend on both components of the strain-rate field. In particular, when we compute the convergent strain-rate, the effective viscosity coefficient should be dominated by the larger component of strike-parallel shear strain-rate. Thus, it is likely that the large strain-rates in the strike-parallel direction will lead to the formation of a weak zone along the plate boundary, through the non-Newtonian (e.g., dislocation creep) response of the lithosphere.

Since the deformation along the plate boundary is dominated by the strike-parallel motion, we can use the results of *England et al.* [1985] to estimate the width of the weak zone and the expected weakening factor. They showed that, for a thin non-Newtonian viscous sheet with stress-exponent n, and strike-parallel velocity

$$u(0,y) = u_o \sin\left(\frac{2\pi y}{\lambda}\right) \tag{1}$$

imposed on the boundary $x = 0$, the strike-parallel velocity component within the sheet decreases with distance x from the boundary approximately as,

$$u \approx u_o \exp\left(-\frac{4\sqrt{n}\pi x}{\lambda}\right) \tag{2}$$

The solution is approximately correct even if the boundary is only driven on a segment of length $\lambda/2$. The exponential decay in the strike-parallel velocity, corresponds to a decay in the strike-parallel strain-rate away from the boundary,

$$\dot{\varepsilon} \propto \exp\left(-\frac{x}{\alpha}\right) \tag{3}$$

where $\alpha = \frac{\lambda}{4\pi\sqrt{n}}$. For non-Newtonian viscosity, stress is related to strain-rate by,

$$\sigma_{ij} = 2\eta_1\dot{\varepsilon}_{ij} \tag{4}$$

where,

$$\eta_1 = B\dot{\varepsilon}^{\frac{(1-n)}{n}}, \tag{5}$$

where $\dot{\varepsilon}$ without subscripts represents the second invariant of the strain-rate tensor and B is a depth-averaged material constant that may include effects caused by temperature and compositional variation. Because the strain-rate invariant is dominated by the strike-parallel shear (3), the viscosity (5) will therefore increase exponentially with distance away from the strike-slip boundary,

$$\eta_1 = \eta_w \exp\left(\frac{x}{x_w}\right) \tag{6}$$

where, $x_w = \frac{n\alpha}{(n-1)}$.

Far from the boundary, strain-rates are low and the lithosphere is likely to be in the diffusion creep regime, with the stress linearly proportional to the strain-rate (Newtonian viscosity),

$$\sigma_{ij} = 2\eta_0\dot{\varepsilon}_{ij} \tag{7}$$

If we assume that the Newtonian and non-Newtonian mechanisms will act in parallel, than the effective viscosity within the layer is found by summing the strain-rates for each mechanism:

$$\eta_e = \frac{\eta_0\eta_1}{\eta_0 + \eta_1}. \tag{8}$$

In southern California the fault-parallel velocity data (Figure 1E) are best fit by a decaying exponential with a length-scale of $\alpha = 67$ km. For the thin sheet dominated by strike-slip motion, this length-scale implies $\lambda/2 = 730$ km for $n = 3$, the expected stress versus strain-rate index for non-Newtonian deformation of olivine. The length of the San Andreas fault along which there is oblique convergence is only about 300 km, however. The mismatch between model prediction and observation here might be attributed to the approximations used in deriving the thin-sheet equations, because the horizontal length scale is not large compared to the layer thickness, and the strike-normal component of deformation - which decays four times more slowly away from the boundary [*England et al.*, 1985] – is small but not negligible. Because of these uncertainties, we therefore assume that the degree of weakening $f_w = \eta_0/\eta_w$ and the width of the weak zone, x_w, should be independently determined in any model of the convergent deformation, as described in the following section. Regardless of these uncertainties, the exponential decay observed in Figure 1E implies that lithospheric strength decreases towards the shear zone according to some relation like that defined by (6) and (8). This weak zone induced by the strike-parallel deformation may then act to localize deformation in the strike-normal direction, which we compute separately, as described in the following section. Thus the two orthogonal components of deformation are coupled through the non-Newtonian viscous response of the lithosphere.

Convergent Deformation in 2-D Vertical Section

We investigate the convergent component of deformation in 2-D plane-strain using the finite element methods developed by *Houseman and Molnar* [1997], *Molnar et al.* [1998] and *Neil and Houseman* [1999], modified to include a viscosity distribution that varies in the horizontal direction according to equations (6) and (8). The numerical model represents a 2-D section of the crust and lithosphere perpendicular to the strike-slip boundary (Figure 2). The model includes a crustal layer (density, ρ_c; viscosity, η_c), overlying a lithospheric-mantle layer (density, $\rho_m = \rho_a + \Delta\rho$; viscosity, η_m), overlying an asthenosphere (density, ρ_a; viscosity η_a). We assume that the asthenosphere viscosity is negligible compared to η_m or η_c. In general we specify that the weak zone parameters f_w and x_w are the same for both crust and lithospheric mantle, ($f_w = \eta_c/\eta_w(c) = \eta_m/\eta_w(m)$, where η_m and η_c are equivalent to η_0 in 8), so that the crust to lithospheric-mantle viscosity ratio η_c/η_m is constant, independent of x. Within each layer we assume, for simplicity, that density and viscosity are independent of depth. The density difference between the lithosphere and asthenosphere, $\Delta\rho$, is attributed to the difference in mean temperature of mantle lithosphere and asthenosphere and the effect of thermal expansion. For models with a weak zone, viscosity increases away from the center of convergence ($x = D_o$), such that the effective viscosity in each layer is given by Equation 8. **Figure 2.**

Convergence is imposed by fixing the displacement rates on the boundaries initially at $x = 0$ and $x = 2D_o$, at a rate of $u = +U_o/2$ and $u = -U_o/2$ respectively, where U_o is the total convergence rate. We focus on models with a free-slip top boundary ($\sigma_{xy} = 0$ and $v = 0$), although the choice of a zero normal velocity at the surface could inhibit certain modes of lithospheric deformation (e.g., folding, see *Zhong and Zuber* [2000]). The hydrostatic stress field due to the constant density asthenosphere is subtracted from the model, so that the bottom boundary (initially at $y = 0$) is traction-free ($n_x\sigma_{xx} + n_y\sigma_{xy} = n_y\sigma_{yy} + n_x\sigma_{xy} = 0$). Initially we investigate models which are symmetric across the center of convergence. In this case, solutions are obtained for only half the domain ($x = 0$ to D_o) and the boundary at $x = D_o$ is a free-slip boundary ($\sigma_{xy} = 0$ and $u = 0$).

Deformation of the lithosphere in 2-D plane-strain is governed by conservation of mass,

$$\dot{\varepsilon}_{ii} = \frac{\partial u_i}{\partial x_i} = 0, \tag{9}$$

and conservation of momentum,

$$\frac{\partial \sigma_{ij}}{\partial x_j} - \rho g \delta_{iy} = 0, \tag{10}$$

where g is the acceleration due to gravity, ρ is density, the stress tensor is $\sigma_{ij} = p\delta_{ij} + \tau_{ij}$, and δ_{ij} is the Kronecker delta. Because the effective viscosity is dominated by the shear strain-rate, we assume that the convergent strain-rate field may be computed using a Newtonian viscous constitutive relation of the form,

$$\tau_{ij} = 2\eta_e \dot{\varepsilon}_{ij}. \tag{11}$$

The system of Equations 9–11 is solved with the boundary conditions illustrated in Figure 2, and viscosity in each layer given by Equation 8, using a finite element method in a Lagrangian formulation (program *basil*). Boundary conditions and material properties are advected by the creeping flow, except that the x-dependent component of the viscosity distribution is held fixed in the reference frame attached to the center of convergence. The equations are solved using non-dimensional variables (primed):

$$x = Lx' \quad (12)$$

$$\rho = \Delta\rho\rho' \quad (13) \qquad u = \frac{g\Delta\rho L^2}{2\eta_m}u' \quad (16)$$

$$\eta = \eta_m\eta' \quad (14) \qquad t = \frac{2\eta_m}{g\Delta\rho L}t' \quad (17)$$

$$\sigma = g\Delta\rho L\sigma' \quad (15)$$

where L is the lithospheric thickness and t is time. Accuracy of the method has been verified previously [*Neil and Houseman*, 1999] by verification of the computed growth rates in the absence of forced convergence.

Observed topography is an important constraint on the deformation mechanism and the viscosity structure. We compare the observed topography to the computed dynamic topography on the upper surface of the crustal layer. At any time t the computed normal stress σ'_{yy} at $y = L$ is that required to ensure that the vertical displacement $v = 0$. The vertical stress is assumed to be in static equilibrium with a topographic burden of:

$$H = \frac{\Delta\rho L}{\Delta\rho_s}\sigma'_{yy} \quad (18)$$

where $\Delta\rho_s$ is the density difference across the top surface ($\Delta\rho_s = \rho_c - \rho_{air}$, where ρ_{air} is the density of air). It is important to note that the effects of erosion and the elastic response of the lithosphere are not included in these models.

Computational results are dimensionalized using parameters appropriate for the southern California region. Based on observed plate convergence rates we choose $U_o = 20$ mm/yr. The density difference between the lithospheric-mantle and asthenosphere is due to the colder temperature of the lithosphere. For an average temperature difference of 360 K, the average density of the lithospheric-mantle is, $\Delta\rho = \rho_a \alpha \Delta T \approx 30$ kg/m^3 greater than that of asthenosphere (assuming $\alpha = 2.5 \times 10^{-5}$ K^{-1}, $\rho_a = 3300$ kg/m^3). With $g = 10$ m/s^2 and $L = 100$ km, the velocity and time scales defined by equations 16 and 17 then depend on the choice of η_m. In the following section we consider different values of η_m and attempt to constrain this poorly determined parameter by comparison of model predictions with observations. Note, however, that a different choice of $\Delta\rho$, L, or U_o would lead to a different choice of η_m.

The results described below illustrate the dependence of the model deformation history (downwelling formation, crustal thickening, topography, and surface convergent velocity profile) on several aspects of the viscosity structure. Initially we assume that the convergent zone is symmetric, and consider parameter sets (Table 1) that include variations in the lithospheric-mantle viscosity (also referred to as either lithosphere or mantle viscosity), η_m (7.5×10^{19}–3.0×10^{21} Pa s), crust to lithospheric-mantle viscosity ratio (also referred to as crust-mantle viscosity ratio), η_c/η_m (10–100), and the weak zone parameters, f_w (5, 10, 50, 100) and x_w (10, 20, 50, 100 km). **Table 1.**

Numerical Experiments on Symmetric Model

In the absence of forced convergence, instability of the lithosphere may develop in response to an initial perturbation of a stratified density structure, which grows at a rate dependent upon the viscosity and/or density structure, and the wavelength of the initial perturbation [e.g., *Houseman and Molnar*, 1997; *Molnar et al.*, 1998; *Neil and Houseman*, 1999]. In general the initial growth rate of the instability in such models is slow, and the total time for the instability to develop is greater than 10 million years if the lithospheric viscosity is greater than about 2×10^{20} Pa s [*Neil and Houseman*, 1999]. At slower growth rates thermal diffusion may stabilize the layer and prevent instability [*Conrad and Molnar*, 1999; *Houseman and Molnar*, 2001]. If uniform horizontal shortening is imposed the growth rate increases [*Molnar et al.*, 1998], but if convergence is localized in a zone of width comparable to the wavelength of the natural instability, density-driven downwelling is more probable still.

Including a weak zone within the lithosphere has a strong localizing effect on the deformation, increasing the growth rate of the instability for weakening factors as small as 1.5. The effectiveness of the weak zone to focus deformation, and how this deformation manifests in the dynamic topography and convergent velocity profiles, depends not only on the width and relative viscosity of the weak zone, it also depends on the overall strength of the lithospheric layer and the crust-mantle viscosity ratio.

The primary effects of increasing the lithospheric viscosity η_m are: higher topography, decreased growth rate of the instability, thus requiring increased total convergence for the downwelling to reach the same depth in a given time, broadening of the deformation zone, and increased crustal thickening within the weak zone. The four models in Figure 3 (See Table 1 for model parameters), illustrate how the topography, convergent velocity and layer deformation, for models with the same weak zone parameters, depend on η_m and the crust to lithospheric-mantle viscosity ratio, η_c/η_m. **Figure 3.**

Deformation in weak lithosphere models (1 and 2; Figure 3) is soon driven by the downwelling, which develops quickly, reaching a depth of 200 km in less than 1 million years. The convergent velocity profiles show the velocity near the weak zone increasing to a value greater than required by the driving velocity, and this rate increases with time as the downwelling rate increases. The increase in surface convergence is more evident in model 1, as the weaker crust is more easily drawn into the weak zone by the downwelling. Strong lithosphere models (3 and 4; Figure 3), in contrast, are driven further by the imposed convergence, with over 150 km of total convergence before the downwelling reaches 200 km depth. The velocity profiles for these experiments do not vary much with time, and reflect the overall horizontal shortening of the layer, localized within the weak zone.

Surface topography for these models depends on several effects, including: horizontal shortening caused by material being pushed or pulled into the weak zone, local thickening or thinning of the crust and lithospheric-mantle, and the downward pull of the mass anomaly in the downwelling sheet. In the weak lithosphere models, material is being pulled into the weak zone by the downwelling. In model 1, with crust-mantle viscosity ratio $\eta_c/\eta_m = 10$, topography building is dominated by viscous shortening in the crust, increasingly driven by the downwelling in the mantle. In model 2, also with a weak mantle lithosphere but relatively stronger crust ($\eta_c/\eta_m = 100$), crustal shortening in the weak zone occurs at slower rates

(Figure 3B). In this case, the downward pull from the downwelling sheet, although comparable to that in model 1, is better coupled to the surface due to the higher crustal viscosity, and overwhelms the upward push caused by shortening; this combination of driving forces result in a deepening topographic low over the center of the weak zone.

In the strong lithosphere models (3 and 4), material is being pushed into the weak zone faster than it is being pulled down by the downwelling (Figure 3C, D). This deformation is accommodated in the crust primarily by increasing horizontal shortening and thickening. Since the crust is less dense than the lithospheric-mantle, the buoyancy of the thickened crust resists the downward pull of the dense mass in the downwelling and adds to the overall positive topography across the weak zone. The greater amplitude of topography in the strong lithosphere models is in part a consequence of comparing the model predictions after different amounts of imposed convergence. In general surface measurements such as topography and convergent velocity profile may evolve with time. This variation must be kept in mind for the comparisons that follow, and if we are to use observations of deformation to constrain the lithospheric viscosity structure. In all cases we have chosen to compare model predictions at the point when the downwelling first reaches the depth of 200 km, as suggested by tomographic images of seismic velocity variation below the Transverse Ranges.

The extent to which the crust-mantle viscosity ratio affects the topography and convergent velocity profiles depends also on the weak zone parameters. For a broad weak zone ($x_w = 100$ km), the topography profiles for crust-mantle viscosity ratios of 10 and 100 are similar (Figure 4A, model 7 versus 11, solid; model 8 versus 12, dashed). If $f_w = 10$, the topography profiles, only differ significantly within about 25–50 km of the center of convergence, where there is a narrow region of higher topography in the stronger crust model (model 11, Figure 4A). For a narrow weak zone ($x_w = 20$ km), however, increasing the crust-mantle viscosity ratio leads to significantly narrower, higher topography (Figure 4C: model 5 versus 9, solid; and model 6 versus 10, dashed). For both crust-mantle viscosity ratios we see that increasing the weakening factor (f_w) from 10 (solid) to 100 (dashed) decreases the magnitude of topography, while increasing the localization of deformation (Figure 4D). **Figure 4.**

While the crust-mantle viscosity ratio has little effect on the overall shape of the topography profiles for broad weak zones, the convergent velocity profiles can differ significantly for those models with a large weakening factor ($f_w = 100$, dashed). The convergent velocity profile for model 8, with $\eta_c/\eta_m = 10$, shows the deformation driven by the downwelling (increasing convergent velocity toward the center of convergence), while the equivalent profile with a larger crust-mantle viscosity ratio ($\eta_c/\eta_m = 100$, model 12) is driven more by convergence (Figure 4B). Similarly, for models with a narrow weak zone, shortening is more localized for models with a larger crust-mantle viscosity ratio (Figure 4D; model 6 versus model 10).

The profiles in Figure 4 illustrate some of the effects of varying weak zone parameters on topography and convergent velocity profile: 1) increasing f_w decreases topographic amplitude, but localizes shortening more within the weak zone, and 2) decreasing x_w increases and narrows topography, and again localizes shortening more within the weak zone. In the first case (increasing f_w), while the strain-rate is higher in the weak zone, the viscosity is lower, resulting in faster growth of the downwelling and therefore less total convergence, less stress on the surface due to convergence, and lower topography. In the second case (decreasing x_w), deformation is strongly focused within the weak zone by the sharp lateral gradient in viscosity, and the locally greater strain-rates lead directly to higher amplitude topography.

As mentioned above, changing the weak zone parameters affects the development of the lithospheric downwelling, and affects crustal thickening (Figure 5). With $\eta_m = 1.5 \times 10^{21}$ Pa s and $\eta_c/\eta_m = 100$, downwelling develops more quickly (less total convergence before the downwelling reaches 200 km depth) for models with a greater weakening factor (compare A versus B and C versus D, Figure 5). Models with greater x_w also develop faster (compare A versus C, or B versus D, Figure 5), though the effect of f_w is greater than that of x_w. Crustal thickening is greater, and more localized for narrower weak zones. Models 14 and 15 have crustal thickening factors of about 1.5 (ratio of crustal thickness within weak zone, to average crustal thickness outside weak zone) within 25 km of the center of convergence, while models 12 and 13 have thickening factors of 1.1 and 1.3, respectively. The small degree of crustal thickening in model 12 is attributable to the small total convergence prior to development of the downwelling in this experiment with $f_w = 100$. **Figure 5.**

Shortening is strongly focused within the weak zone for models with a greater weakening factor or narrower weak zone, though the effect of x_w is less marked than that of f_w. Topographic amplitude is maximized for models with a narrow weak zone and small weakening factor, and conversely minimized for models with a broad weak zone and large weakening factor (compare Figure 5A–D). The main control on the amplitude of topography at the time the downwelling reaches 200 km depth is the total amount of convergence. If the weak zone parameters lead to a lower overall lithospheric viscosity, then the downwelling will develop quickly and there will be little convergence and low topography.

Oblique Convergence Across the San Gabriel Mountains

In order to explain the observed deformation along the oblique convergent margin of the San Gabriel Mountains in southern California, model predictions must satisfy the observed deformation, including: present-day convergent velocity profile, and topography, crustal thickening and lithospheric downwelling developed within the period since convergence began (5 Ma), at the plate convergence rate (20 mm/yr). The numerical results described above demonstrate strong trade-offs between the height and shape of topography, the total amount of convergence, the degree of focusing of horizontal shortening within the weak zone, and the distribution of crustal thickening. Initial inspection suggests that only a small subset of the models investigated can provide a reasonable match to all of these observations.

We summarize the deformation measures for the set of models with a relatively strong crust ($\eta_c/\eta_m = 100$) in Figure 6. Parameter values that lead to predictions consistent with the relevant observation in southern California are indicated by the gray shaded region on each of these maps. Firstly, in order for the downwelling to reach 200 km depth in less than 5 Ma at a convergence rate of 20 mm/yr, the total convergence needs to be less than 100 km (50 km in the half-domain represented in the symmetric models). This constraint is met by a range of weakening factors, which depends on the lithospheric viscosity, but shows little dependence on the weak zone width (Figure 6A, B). **Figure 6.**

The observed topography in the San Gabriel Mountains averages 1.5 km, with peaks greater than 3.0 km [*Blythe et al.*, 2000]. Model topography of about 2.5 km is obtained for $\eta_m = 1.5 \times 10^{21}$ Pa s, over a range of weakening factors and weak zone widths in the range 20 to 50 km (Figure 6C, D). A similar constraint is provided by the observed crustal thickness variation from 30 to 40 km beneath the San Gabriel Mountains. Assuming that this variation in Moho depth is attributed to the recent deformation, we require a crustal thickening factor of about 1.3 (Figure 6E, F).

The strongest constraint on the weak zone parameters comes from the width of the topographic high. The observed width of the uplift in the San Gabriel Mountains is less than 50 km (Figure 1D). For the large weakening factors required to match the net convergence constraint, the width of topography is not strongly affected by the lithospheric viscosity. However, only models with a weak zone in the range $x_w = 20$ to 50 km can reproduce the narrow width (15–25 km full width at half-height) of the topographic high (Figure 6G, H).

The final observation that constrains the viscosity structure is the convergent velocity profile, which shows a decay in convergent velocity over a length scale of 50 to 80 km (Figure 1E). This shortening length scale, estimated from model profiles as the distance across which the convergent velocity decreases by a factor of e, is only fit by models with high lithospheric-mantle viscosity ($\eta_m \geq 1.5 \times 10^{21}$ Pa s) as shown in Figure 6I, but is equally well-matched by weak zones with widths from 20 to 100 km for $f_w = 50$ and $f_w = 100$ (Figure 6J).

Both the topography and convergent velocity profiles are sensitive to variations in the weak zone parameters. Therefore, matching all these observations simultaneously is difficult, and indeed requires some compromise. The best fitting symmetric model, estimated by inspection (with parameters indicated by the star in Figure 6) is compared to the profiles of topography and convergent velocity from southern California in Figure 7. Model 10 assumes

$\eta_m = 1.5 \times 10^{21}$ Pa s, $\eta_c/\eta_m = 100$, a weak zone width of $x_w = 20$ km, and weakening factor $f_w = 100$. While this model predicts narrow, high topography, the prediction overestimates the observed width. The prediction of the convergent velocity profile is within observational error, though it probably underestimates the width of the convergence. The tendency towards broader, lower topography for models with a lower crust-mantle viscosity ratio, would make it even more difficult to match the above set of observations, by requiring an even higher lithosphere viscosity, which would increase the convergence times. Therefore, only models with a relatively large crust-mantle viscosity ratio ($\eta_c/\eta_m = 100$) are able to reproduce the high, narrow topography observed across the San Gabriel Mountains. **Figure 7.**

One of the striking features of the topography across the San Gabriel Mountains is the asymmetry of the profile. The highest topography is shifted about 20 km south of the San Andreas Fault and the average height of topography north of the San Andreas fault is 1 km higher than in the Los Angeles Basin. While this asymmetry, may reflect processes not included in our models, such as erosion and brittle faulting, we briefly explore what modifications to the lithospheric structure might explain this feature. Asymmetry is investigated using a full-width model ($x = 0 - 2D_o$, $D_o = 600$ km) in which the viscosity and density structure may be asymmetric with respect to the center of convergence ($x = D_o$).

In order to match the asymmetry in the topography and velocity profiles, we introduced changes to the parameters of the best-fit symmetric model (10) as follows: First, in order to match the 1 km offset in average topography from south to north of the convergent zone, we reduce the average density of the crustal layer north of the weak zone by 50 kg/m^3 compared to that in the Los Angeles Basin ($x = 0$ to D_o in the model; Figure 8). This difference in average density is consistent with estimates based on crustal exposures [*Wooley and Langenheim,* 2001] and provides an explanation for the difference in average elevation of these two regions. Second, in order to match the offset in location between the topography and the present day center of convergence, we shift the center of the weak zone 30 km south of this density discontinuity. This assumption approximately represents the inferred migration of the plate boundary northward from the San Gabriel Fault, which accommodated over 40 km of strike-slip displacement between 13 and 4 Ma, to the present day San Andreas Fault [*Nourse,* 2002; *Powell and Weldon,* 1992]. The region to the south of the San Andreas Fault therefore may have been subject to greater strike-parallel strain (and thus weakening) than the region to the north. **Figure 8.**

In order to match the asymmetry of the velocity and topography profile, adjustments to the relative crustal viscosity south of the San Andreas Fault, and to the weak zone parameters, were also investigated. The topography of the San Gabriel Mountains is much steeper on the south side, than on the north side, indicating a stronger viscosity gradient to the south. However, increasing the viscosity on the south side, increases the height and narrows the topography. Therefore, an increase of the crustal viscosity must be offset by a decrease of the mantle viscosity in order to maintain the small net convergence and preserve the height of topography while making the slope steeper. This difference in crustal viscosity is consistent with seismic observations that indicate the lower crust of the Los Angeles Basin is mafic in composition, while the lower crust of the Mojave Desert is felsic to intermediate [*Fuis et al.,* 2001]. Based on experimental data at lower crustal conditions, the strength of mafic rocks with a olivine-dominate rheology is expected to be several orders of magnitude greater than felsic rock with a quartzite-dominated rheology [*Kohlstedt et al.*, 1995; *Chen and Molnar*, 1983].

Using the results from a large set of symmetric models that we investigated, we find that we can increase the crust-mantle viscosity ratio on the south side (of $D_o - 30$ km) from 100 to 200, and yet maintain the required topographic elevation if we also decrease the lithospheric viscosity η_m to 7.5×10^{20} Pa s. At the same time, to better match the slopes of topography and the convergent velocity profile, we decrease the weakening factor f_w from 100 to 50. The final asymmetric model (Model A in Figure 8) provides an improved fit to the observed topography, the convergent velocity profile, the net convergence needed for the downwelling to reach 200 km depth (30 km), and the maximum crustal thickening factor (1.34). To illustrate the influence of the increased crust-mantle viscosity ratio to the south, Figure 8 also shows the topography and velocity profiles for model B, which is identical to model A, except that is has a uniform crust-mantle viscosity ratio. Model B has lower, broader topography and under predicts the increase in convergent velocity on the south side.

Conclusions

The model presented here investigates the effect of a non-Newtonian lithospheric viscosity in the plate boundary region. Strike-parallel and strike-normal deformations are coupled by the non-linear viscous constitutive relation. We have made several important simplifications, however, to keep the problem tractable. Other components of deformation are omitted, including the elastic response of the lithosphere, brittle failure of the crust, and erosion. While the elastic response of the lithosphere will act to distribute loads at short wavelengths leading to broader topography, brittle deformation and erosion will likely help to further localize deformation. The parameters that we have estimated for the low viscosity region may thus require amendment if these other processes are included in the model. In particular, pre-existing heterogeneities, erosional processes, or the development of faults to accommodate uplift may all play a role in creating the observed asymmetry in the topography.

Although we have examined a relevant range of the density and strength contrasts between crust and lithospheric-mantle layers, we have also, for simplicity, assumed that these layers are each vertically homogeneous. The effect on our experiments of a low viscosity channel at the base of the crust is uncertain. *Royden* [1996] showed that a ductile lower crustal layer existing before convergence begins, results in broad, muted topography, while the development of a ductile lower crust during deformation leads to only slightly less topography at short times (1–4 myrs) compared to uniform crust models. Experiments to examine this possibility are needed, but were considered beyond the scope of this study. Our inferred model parameters should therefore be interpreted in terms of a depth-averaged viscosity, which is by definition less than the peak viscosity in each layer. In addition, these values are valid only in the domain of the model constrained by observations (250 km wide). Although the lithosphere in general probably has much greater viscous strength than we infer for this plate boundary region, we surmise that the relatively low strengths cited here are a consequence of the history of deformation in this region.

With those caveats, the models presented here illustrate some of the possible variation in lithospheric deformation that may develop in an oblique continental convergent margin. Our fundamental assumption is that strike-parallel motion may focus convergent deformation by creating a lithospheric weak zone. For a fixed set of weak zone parameters, we have found that the shape and height of topography, Moho displacement, and growth rate of the instability depend firstly on the lithospheric-mantle viscosity and on the crust-mantle viscosity ratio: increasing the lithospheric-mantle viscosity and/or the crust-mantle viscosity ratio increases topography, increases Moho displacement, and decreases the growth-rate of the associated gravitational instability. For a fixed lithospheric-mantle viscosity and crust-mantle viscosity ratio, decreasing the weak zone width x_w, increases topographic elevation and narrows the zone of shortening and high topography. Similarly, increasing the weakening factor f_w increases the growth rate of the instability and decreases topography, but has only a weak effect on the width of high topography.

The observations of topography, Moho displacement and convergent velocity profile for the San Gabriel Mountains region of southern California can be matched by a lithospheric instability model with a lithospheric-mantle viscosity of about 7.5×10^{20} Pa s, a crust-mantle viscosity ratio $\eta_c/\eta_m = 100$–200, and narrow weak zone defined by width, $x_w = 20$ km, and weakening factor, $f_w = 50$. This model includes a difference in average crustal density between Los Angeles and Mojave regions and a weak zone centered 30 km south of the San Andreas Fault Zone, consistent with geological observations and history of deformation. The lithospheric viscosity estimates that we obtain are consistent with those estimated independently for the depth-averaged lithospheric viscosity in the southern California region by *Flesch et al.* [2000] (1–5×10^{21} Pa s decreasing by a factor of 10 near the San Andreas Fault). Those authors were unable, however, to assess the contrast between average viscosities of crust and mantle lithosphere. Like *Houseman et al.* [2000] we conclude that the crust must be stronger than the lithospheric mantle in Southern California. Unlike them we find that the average effective crustal viscosity is as much as two orders of magnitude greater than that of the mantle lithosphere in this region.

We have presented a rationale for a lithospheric weak zone approximately centered on the plate boundary in the Transverse Ranges of southern California. The width of the weak zone that one would infer from the strike-parallel geodetic displacement profile is, however, too wide here, by at least a factor of 2, for consistency with the thin sheet model with $n = 3$, on which we base our argument. The value of $x_w = 67$ km inferred from Figure 1E also may be too large to allow a satisfactory prediction of the observed narrow width of the topography. The explanation of this discrepancy could lie in our assumptions concerning the formation of the weak zone, the effective constitutive relation of the lithosphere (including possibly arbitrary spatial variation of the viscous strength parameters), the interpretation of the geodetic strain-rate data, or the processes that are assumed to have created the topography. This discrepancy remains unresolved at this time.

Our approximate two dimensional models of oblique convergence have demonstrated that lithospheric instability may be localized by plate boundary geometry interacting with a non-Newtonian viscosity law. There is, however, significant along-strike variability on the obliquely convergent plate boundary segment we have studied. In particular, the fast seismic velocity anomaly lies further south of the San Andreas Fault in the west [*Kohler*, 1999], and lies beneath the San Bernadino Mountains north of the San Andreas Fault in the east. Full three-dimensional models that allow oblique convergent margin deformation to be investigated without the kind of approximations used here, but incorporating along-strike variation of properties may be the next important step in understanding partitioning of deformation in these types of collision zones.

Acknowledgments. We thank Louis Moresi, Russell Pysklywec and Shijie Zhong for their thoughtful reviews.

References

Beaumont, C., P. Fullsack, and J. Hamilton, Styles of crustal deformation caused by subduction of the underlying lithosphere, *Tectonophysics*, *232*, 119–132, 1994.

Bird, P., Initiation of intracontinental subduction in the Himalayas, *J. of Geophys. Res.*, *83*, 4975–4987, 1978.

Bird, P., Continental delamination and the Colorado Plateau, *J. of Geophys. Res.*, *84*, 7561–7571, 1979.

Bird, P., and R. W. Rosenstock, Kinematics of present crust and mantle flow in southern California, *Geological Society of America Bulletin*, *95*, 946–957, 1984.

Blythe, A. E., D. W. Burbank, K. A. Farley, and E. J. Fielding, Structural and topographic evolution of the central Transverse Ranges, California, from apatite fission-track, (U-Th)/He and digital elevation model analyses, *Basin Research*, *12*, 97–114, 2000.

Chen, W.-P., and P. Molnar, Focal depths of intracontinental and intraplate earthquakes and their implications for the thermal and mechanical properties of the lithosphere, *J. of Geophys. Res.*, *88*, 4183–4214, 1983.

Conrad, C. P., and P. Molnar, Convective instability of a boundary layer with temperature- and strain-rate-dependent viscosity in terms of ’available buoyancy’, *Geophys. J. Int.*, *139*, 51–68, 1999.

Crustal Deformation Working Group, Horizontal deformation velocity map, version 2.0, *Tech. rep.*, Southern California Earthquake Center, Los Angeles, 1998.

de Mets, C., R. G. Gordon, D. F. Argus, and S. Stein, Current plate motions, *Geophys. J. Int.*, *101*, 425–478, 1990.

England, P., G. Houseman, and L. Sonders, Length scales for continental deformation in convergent, divergent, and strike-slip environments: Analytical and approximate solutions for a thin viscous sheet model, *J. of Geophys. Res.*, *90*, 3551–3557, 1985.

Flesch, L. M., W. E. Holt, A. J. Haines, and B. Shen-Tu, Dynamics of the Pacific-North American plate boundary in the Western United States, *Science*, *287*, 834–836, 2000.

Fuis, G. S., Western margin of North America – a synthesis of recent seismic transects, *Tectonophysics*, *288*, 265–292, 1998.

Fuis, G. S., T. Ryberg, N. J. Godfrey, D. A. Okaya, and J. M. Murphy, Crustal Structure and tectonics from the Los Angeles basin to the Mojave Basin, southern California, *Geology*, *29*, 15–18, 2001.

Gerbault, M., S. Henrys, and F. Davey, Numerical models of lithospheric deformation forming the Southern Alps of New Zealand, *J. of Geophys. Res.*, *108*, 2341,doi:10.1029/2001JB001,716, 2003.

Hadley, D., and H. Kanamori, Seismic structure of the Transverse Ranges, California, *Geological Society of America Bulletin*, *88*, 1469–1478, 1977.

Hafner, K., R. W. Clayton, and E. Hauksson, Mid and lower-crustal structure beneath the San Gabriel Mountains, CA (LARSE)(abstract), *Eos Transactions AGU Fall Meeting Supplement*, *46*, F738, 1996.

Hearn, T. M., and R. W. Clayton, Lateral velocity variations in Southern California, II, Results for the lower crust from P_n waves, *Bulletin of the Seismological Society of America*, *76*, 511–529, 1986.

Houseman, G., and P. Molnar, Mechanisms of lithospheric rejuvenation associated with continental orogeny, in *Continental Reactivation and Reworking*, edited by J. A. Miller, R. E. Holdsworth, I. S. Buick, and M. Hand, vol. 184, pp. 13–38, The Geological Society of London, London, 2001.

Houseman, G. A., and P. Molnar, Gravitational Rayleigh-Taylor instability of a layer with nonlinear viscosity and convective thinning of continental lithosphere, *Geophys. J. Int.*, *128*, 125–150, 1997.

Houseman, G. A., D. P. McKenzie, and P. Molnar, Convective instability of a thickened boundary layer and its relevance for the thermal evolution of continental convergent belts, *J. of Geophys. Res.*, *86*, 6115–6132, 1981.

Houseman, G. A., E. A. Neil, and M. D. Kohler, Lithospheric instability beneath the Transverse Ranges of California, *J. of Geophys. Res.*, *105*, 16,237–16,250, 2000.

Hu, G., W. Menke, and C. Powell, Polarization tomography for P wave velocity structure in southern California, *J. of Geophys. Res.*, *99*, 15,245–15,256, 1994.

Humphreys, E. D., and B. H. Hager, A kinematic model for the Late Cenozoic development of Southern California crust and upper mantle, *J. of Geophys. Res.*, *95*, 19,747–19,762, 1990.

Humphreys, E. D., and R. W. Clayton, Tomographic image of the southern California mantle, *J. of Geophys. Res.*, *95*, 19,725–19,746, 1990.

Kohler, M. D., Coupled crust-mantle deformation beneath the San Gabriel Mountains in the Southern California Transverse Ranges, *J. of Geophys. Res.*, *104*, 15,025–15,041, 1999.

Kohler, M. D., and P. M. Davis, Crustal thickness variations in southern California from Los Angeles Regional Seismic Experiment passive phase teleseismic travel times, *Bulletin of the Seismological Society of America*, *87*, 1130–1344, 1997.

Kohlstedt, D. L., B. Evans, and S. J. Mackwell, Strength of the lithosphere: constraints imposed by laboratory experiments, *J. of Geophys. Res.*, *100*, 17,587–17,602, 1995.

Molnar, P., G. A. Houseman, and C. P. Conrad, Rayleigh-Taylor instability and convective thinning of mechanically thickened lithosphere: effects of non-linear viscosity decreasing exponentially with depth and of horizontal shortening of the layer, *Geophys. J. Int.*, *133*, 568–584, 1998.

Neil, E. A., and G. A. Houseman, Rayleigh-Taylor instability of the upper mantle and its role in intraplate orogeny, *Geophys. J. Int.*, *138*, 89–107, 1999.

Nourse, J. A., Middle Miocene reconstruction of the central and eastern San Gabriel Mountains, southern California, with implications of evolution of the San Gabriel fault and Los Angeles basin, in *Crustal Evolution of the Southwestern United States*, edited by A. Barth, Special Paper 365, Geological Society of America, Boulder, Colorado, 2002.

Powell, C. A., and B. T. Mitchell, Relative array analysis of the southern California lithosphere, *J. of Geophys. Res.*, *99*, 15,257–15,275, 1994.

Powell, R. E., and R. J. Weldon, Evolution of the San Andreas Fault, *Annual Reviews of Earth and Planetary Sciences*, *20*, 431–468, 1992.

Raikes, S. A., Regional variations in upper mantle structure beneath southern California, *Geophys. J. Royal Astro. Soc.*, *63*, 187–216, 1980.

Royden, L., Coupling and decoupling of crust and mantle in convergent orogens: inplications for strain partitioning in the crust, *J. of Geophys. Res.*, *101*, 17,679–17,705, 1996.

Sheffels, B., and M. McNutt, Role of subsurface loads and regional compensation in the isostatic balance of the Transverse Ranges, California: evidence for intracontinental subduction, *J. of Geophys. Res.*, *91*, 6419–6431, 1986.

Willet, S. D., and C. Beaumont, Subduction of Asian lithosphere mantle beneath Tibet inferred from models of continental collision, *Nature*, *369*, 642–645, 1994.

Wooley, R. J., and V. E. Langenheim, Gravity data along LARSE (Los Angeles Regional Seismic Experiment) Line II, southern California, *Tech. Rep. Open-File Report 01-375*, U.S. Geological Survey, Menlo Park, CA, 2001.

Zhong, S., and M. T. Zuber, Crustal compensation during mountain building, *Geophys. Res. Lett.*, *27*, 3009–3012, 2000.

M. I. Billen, Department of Geology, U. C. Davis, Davis, CA 95616, USA. (billen@geology.ucdavis.edu)

Gregory A. Houseman, School of Earth Sciences, University of Leeds, Leeds, LS2 9JT, UK. (greg@earth.leeds.ac.uk)

Received ______________________

This manuscript was prepared with AGU's LaTeX macros v5, with the extension package 'AGU^{++}' by P. W. Daly, version 1.6b from 1999/08/19.

Figure Captions

Figure 1. (A) Topography in Southern California (from USGS, 90 minute DEM), with arrows indicating components of horizontal velocity from GPS measurements, relative to stable North America [*Crustal Deformation Working Group*, 1998]: white - normal to, and black - parallel to the San Andreas Fault (SAF, thin white line). Thick white line denotes location of cross section for topography and velocity profiles across the Los Angeles Basin (LAB) and San Gabriel Mountains (SGM) region of the Eastern Transverse Ranges. **(B)** Fault-normal velocity projected onto the profile in A, relative to a fixed San Andreas Fault (SAF at 0 km). **(C)** Fault-parallel velocity relative to a fixed San Andreas Fault. **(D)** Topography on same profile. **(E)** Best fit (black line) to log($25 - u$ mm/yr) versus $-x$, where u (velocity) and x (distance) are the measurements shown in (C) relative to the stable Pacific Plate, for data southwest of SAF ($x < 0$).

Figure 2. Numerical Model Geometry. **(A)** Initial density and viscosity distributions, and boundary conditions, for numerical models of convergence with a weak zone. The center of convergence is at $x = D_o$. Gray shading indicates variation in viscosity (layers and lateral gradient) and density (layers only). **(B)** Example viscosity profiles (assuming $L = 100$ km): black-solid, $f_w = 10$, $x_w = 20$ km; black-dashed, $f_w = 100$, $x_w = 20$ km; gray-solid, $f_w = 10$, $x_w = 100$ km; gray-dashed, $f_w = 100$, $x_w = 100$ km;

Figure 3. Influence of mantle viscosity and crust-to-mantle viscosity ratio on deformation with fixed weak zone parameters ($x_w = 100$ km, $f_w = 10$). In each column, top to bottom: Convergent velocity profile, topography, layer deformation, and crustal viscosity profile (relative to mantle viscosity), at three time steps (t_1-light gray, t_2-dark gray, t_3-black). For the final time-step the crust-lithosphere boundary is also shown with the layer deformation. **(A–B)** Models 1 and 2 with $\eta_m = 7.5 \times 10^{19}$ Pa s. **(C–D)** Models 3 and 4 with $\eta_m = 3 \times 10^{21}$ Pa s. Note differences in vertical scales for topography and velocity profiles.

Figure 4. Influence of weak zone parameters and crust-mantle viscosity ratio on topography and convergent velocity profiles, for fixed lithospheric viscosity ($\eta_m = 1.5 \times 10^{21}$ Pa s). Profiles shown at time downwelling reaches 200 km depth, t_i. **(A–B)** Models 7, 8, 11, and 12 ($x_w = 100$ km), at $t_i = 5.4$, 1.2, 5.3, and 1.2 myr, respectively. **(C–D)** Models 5, 6, 9 and 10 ($x_w = 20$ km) at $t_i = 7.8$, 1.5, 7.3 and 1.4 myr, respectively. Lines are coded for model numbers and parameter values as follows: Solid-black (5 and 7), dashed-black (6 and 8), solid-gray (9 and 11), dashed-gray (10 and 12), solid $f_w = 10$, dashed $f_w = 100$, black $\eta_c/\eta_m = 10$, gray $\eta_c/\eta_m = 100$.

Figure 5. Influence of weak zone parameters (x_w and f_w) for experiments with ($\eta_m = 1.5 \times 10^{21}$ Pa s) and ($\eta_c/\eta_m = 100$). Panels are the same as Figure 3. **(A–D)** Models 12 to 15, with x_w and f_w as labeled on bottom panel. Note differences in vertical scale for topography profiles.

Figure 6. Summary of deformation measures mapped on the f_w vs η_m and f_w vs x_w planes, for experiments with ($\eta_c/\eta_m = 100$). All values are measured when the instability reaches 200 km depth. **(A, C, G, E, I)** Left column, $x_w = 20$ km. **(B, D, F, H, J)** Right column, $\eta_m = 1.5 \times 10^{21}$ Pa s. Gray regions indicate values consistent with southern California observations. Star indicates the symmetric model which, by inspection, best fits the set of observations.

Figure 7. Comparison of observed topography **(A)** and convergent velocity **(B)** with predictions of Model 10 (gray lines). Note, for comparison of symmetric models to observed topography, the peak observed topography is aligned with the center of convergence.

Figure 8. Comparison of observations and predictions of asymmetric Model A ($\eta_c/\eta_m = 200$ for $x = 0$ to $D_o - 30$ km; $\eta_c/\eta_m = 100$ for $x = D_o - 30$ km to $2D_o$; $D_o = 600$ km) and Model B ($\eta_c/\eta_m = 100$ for $x = 0$ to $2D_o$; $D_o = 600$ km) at the time the instability reaches 200 km depth. **(A)** Topography: observed (black), Model A (gray) and Model B (gray-dashed). **(B)** Convergent velocity: observed (black dots,) Model A (gray line) and Model B (gray-dashed). **(C)** Density (gray shading) and layer deformation in vicinity of weak zone for Model A. Density discontinuity is initially located at $x_c = D_o$ km with $\rho_c(S) - \rho_c(N) = 50$ kg/m^3. **(D)** Viscosity (gray shading) and layer deformation in vicinity of weak zone for Model A.

Tables

Model	η_m (Pa s)	η_c/η_m	x_w (km)	f_w
1	7.5×10^{19}	10	100	10
2	7.5×10^{19}	100	100	10
3	3.0×10^{21}	10	100	10
4	3.0×10^{21}	100	100	10
5	1.5×10^{21}	10	20	10
6	1.5×10^{21}	10	20	100
7	1.5×10^{21}	10	100	10
8	1.5×10^{21}	10	100	100
9	1.5×10^{21}	100	20	10
10	1.5×10^{21}	100	20	100
11	1.5×10^{21}	100	100	10
12	1.5×10^{21}	100	100	100
13	1.5×10^{21}	100	100	5
14	1.5×10^{21}	100	10	100
15	1.5×10^{21}	100	10	5
A	7.5×10^{20}	200, 100	20	50
B	7.5×10^{20}	100	20	50

Table 1. Summary of parameters for symmetric models (1-15) and asymmetric model (A-B). For Model A, the two values of η_c/η_m are for $x = 0$ to $D_o - 30$ km and $x = D_o - 30$ to $2D_o$, respectively ($D_o = 600$ km).

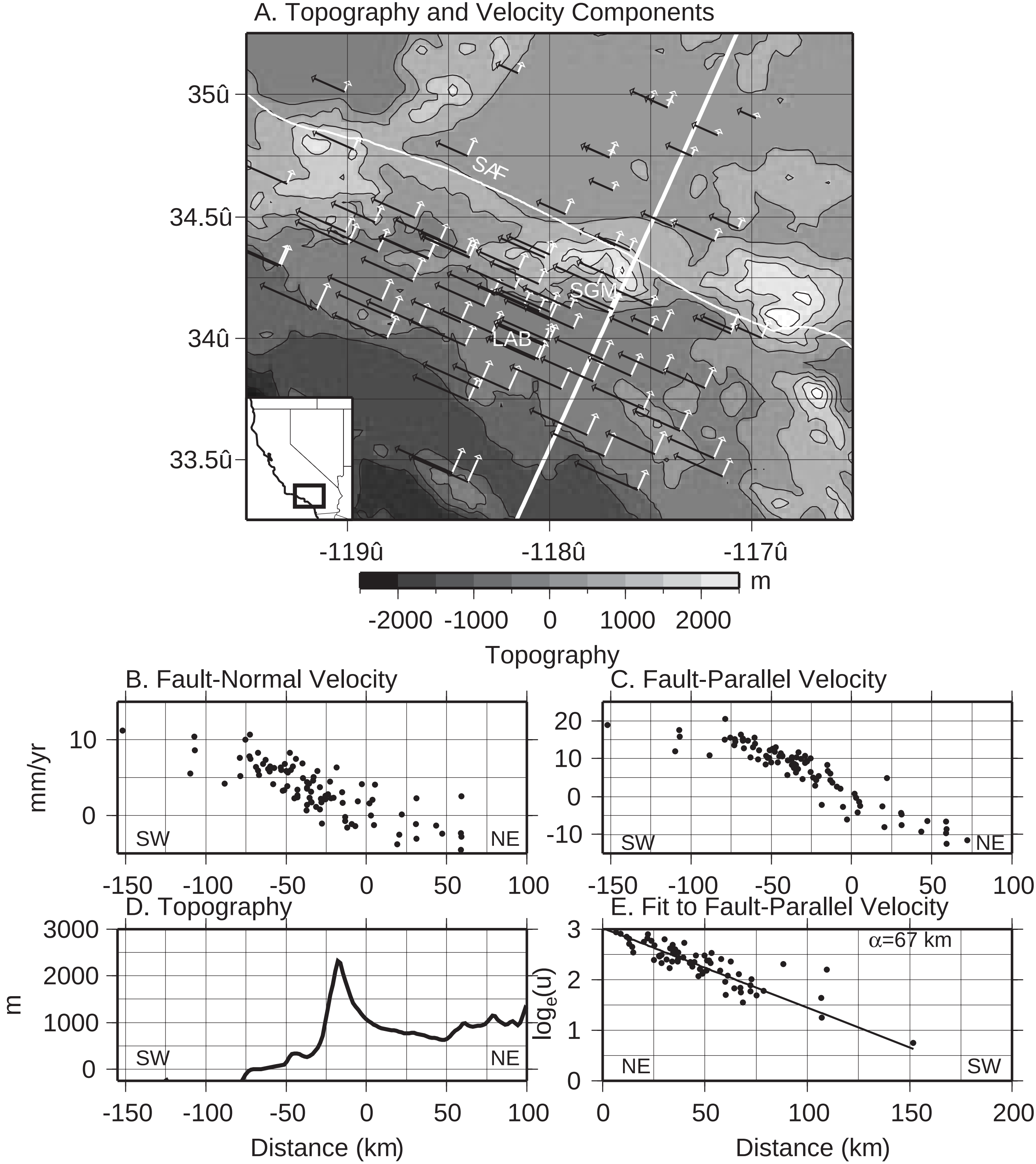

Billen and Houseman, Figure 1

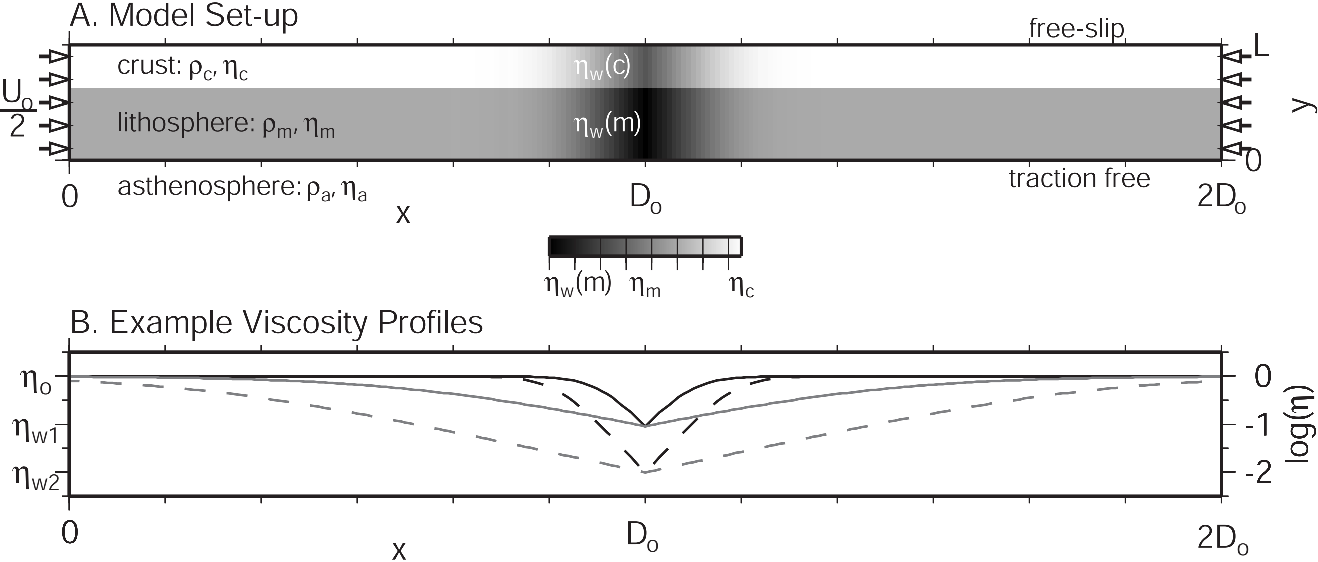

Billen and Houseman, Figure 2

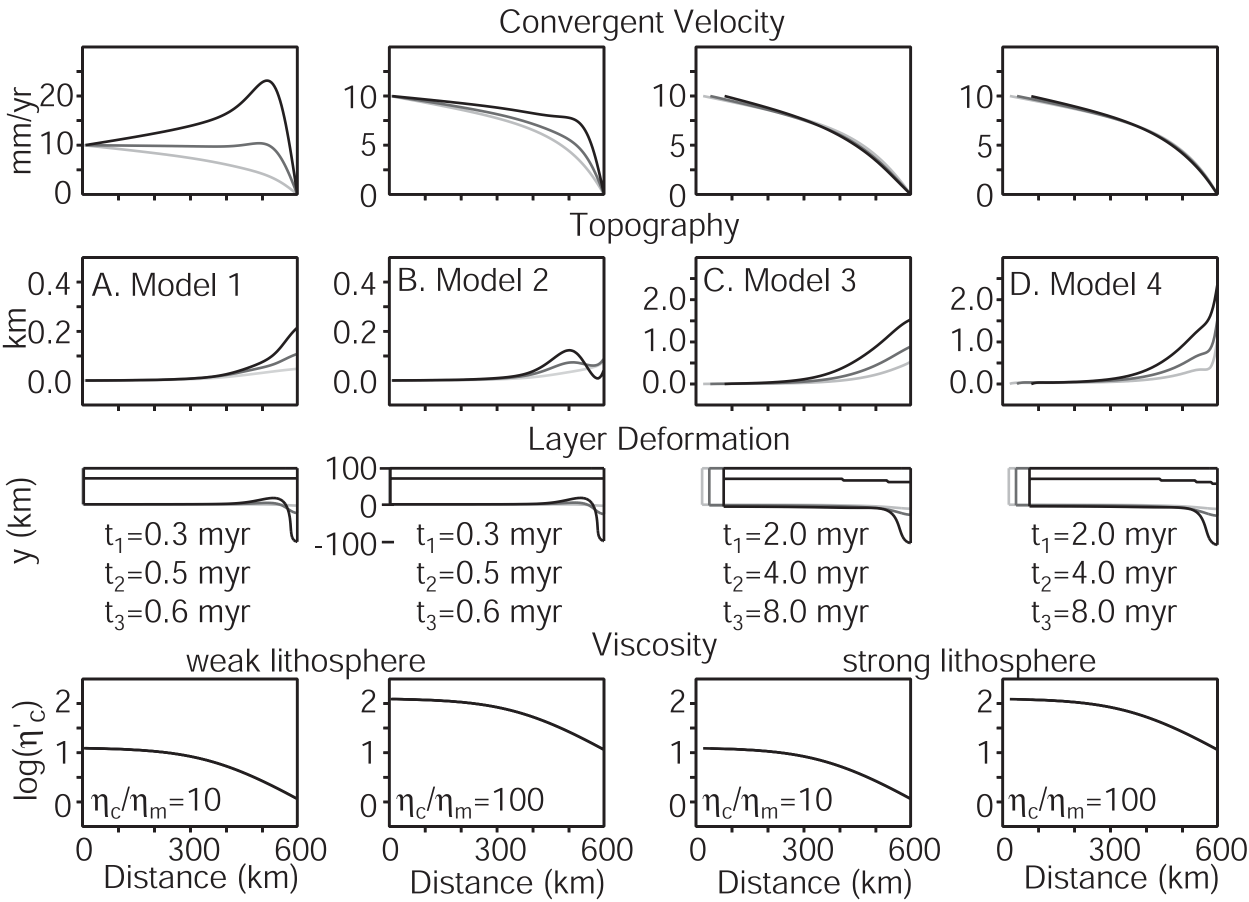

Billen and Houseman, Figure 3

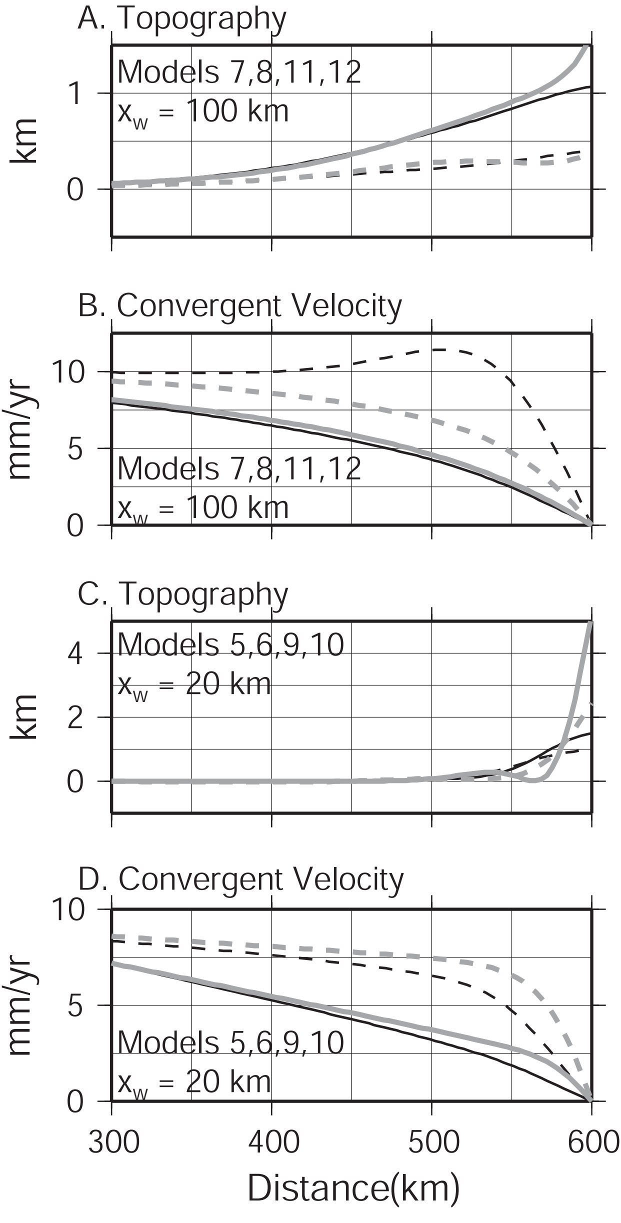

Billen and Houseman, Figure 4

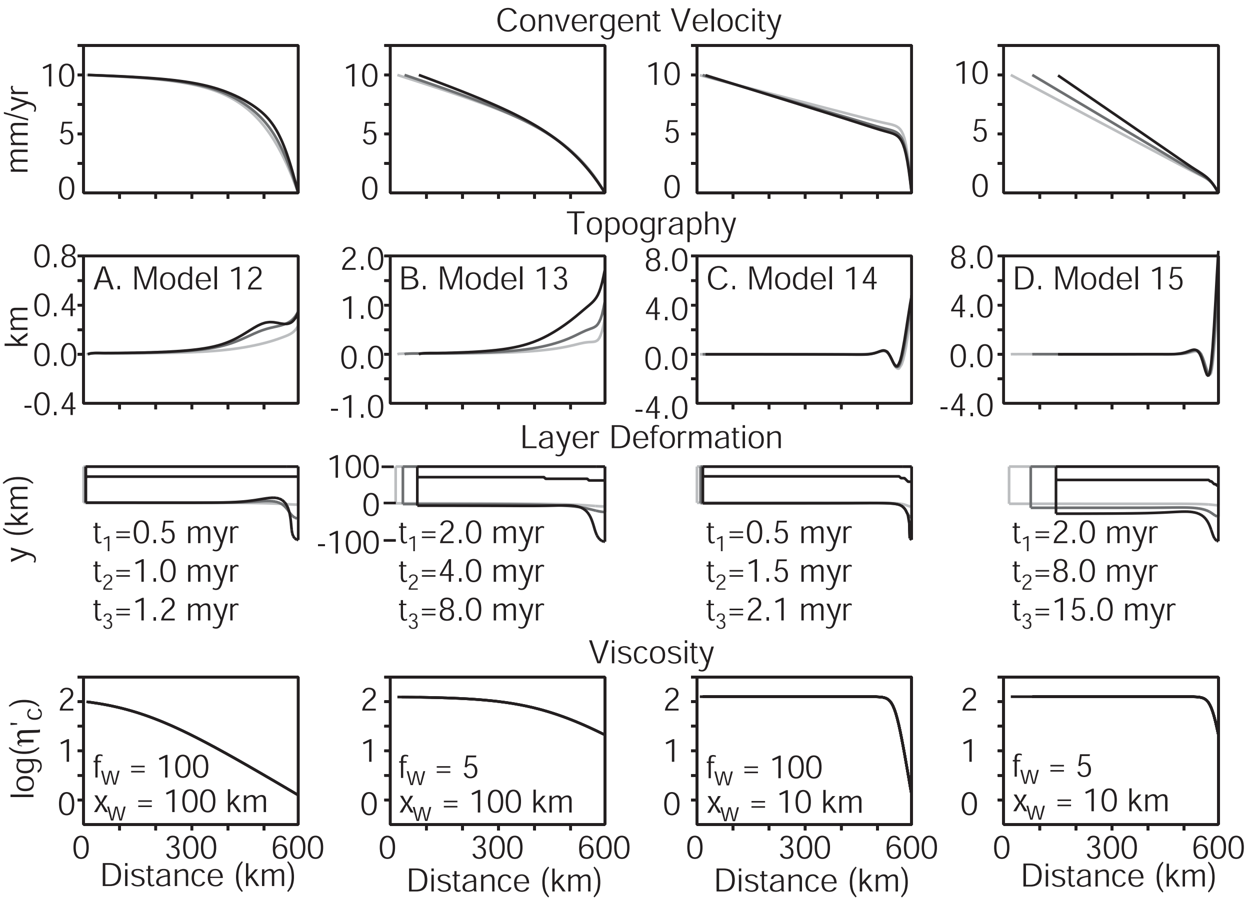

Billen and Houseman, Figure 5

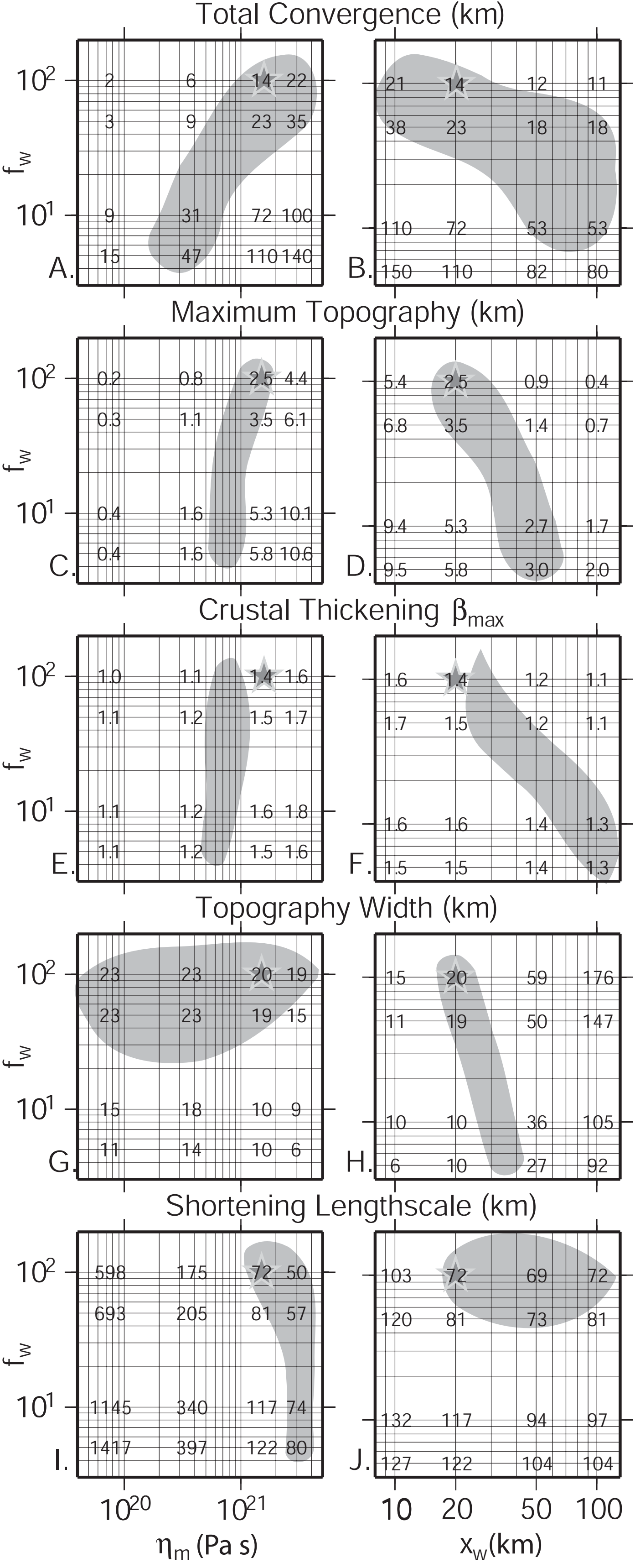

Billen and Houseman, Figure 6

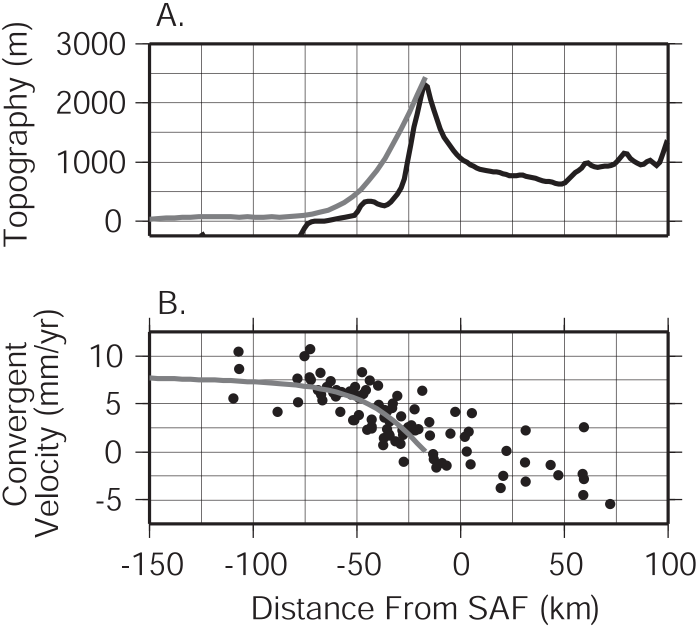

Billen and Houseman, Figure 7

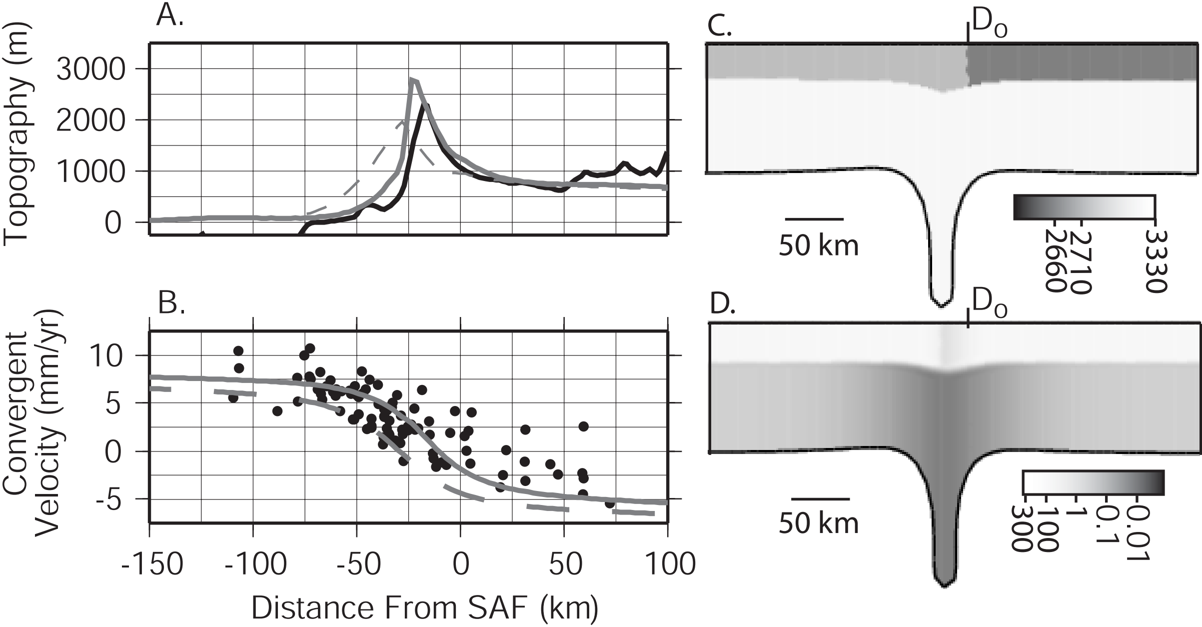

Billen and Houseman, Figure 8